

Strain accumulation across strike-slip faults: Investigation of the influence of laterally varying lithospheric properties

Wen-Jeng Huang¹ and Kaj M. Johnson²

Received 2 May 2012; revised 1 August 2012; accepted 8 August 2012; published 25 September 2012.

[1] We use boundary element methods to develop antiplane, strike-slip earthquake cycle models consisting of faulting in an elastic plate with possibly different thickness and stiffness on either side of the fault overlying a linear, Maxwell viscoelastic substrate. We show that isolated plate models that neglect the coupling of the plate to the underlying substrate might significantly overpredict the asymmetry in deformation across the fault. We also show that flow in a low-viscosity channel in the lower crust could significantly contribute to the asymmetry. Through a fully probabilistic scheme, we invert geodetic data across three strike-slip fault systems for effective elastic thickness and elastic stiffness on both sides of the fault using geological and geophysical constraints. For the Renun segment of the Great Sumatra fault, inversion results show the elastic layer on the east side is stiffer than the west side but the effective elastic thicknesses are not resolvable. For the Carrizo segment of the San Andreas fault, the inversion results slightly favor a thicker elastic layer on the east side (~ 2.2 times) but stiffer layer on west side (~ 1.2 times); however, uniform effective elastic thickness and stiffness cannot be ruled out. For the Aksay segment of the Altyn Tagh fault in northern Tibet, inversion results show the effective elastic crust of the Tarim Basin must be stiffer and thicker than the effective elastic crust of the Tibetan Plateau to the south, but the viscosity of a hypothesized mid-crustal Tibetan channel is not resolvable.

Citation: Huang, W.-J., and K. M. Johnson (2012), Strain accumulation across strike-slip faults: Investigation of the influence of laterally varying lithospheric properties, *J. Geophys. Res.*, 117, B09407, doi:10.1029/2012JB009424.

1. Introduction

[2] Large strike-slip faults commonly juxtapose materials with different physical properties. Observed fault damage asymmetry [Mitchell *et al.*, 2011] and asymmetric distribution of aftershocks [Zaliapin and Ben-Zion, 2011] may be attributed to a contrast in elastic properties across faults. The asymmetry in elastic properties across faults has been shown to be an important factor in the dynamics of earthquake ruptures on bimaterial interfaces [Ampuero and Ben-Zion, 2008; Ben-Zion and Andrews, 1998; Andrews and Ben-Zion, 1997].

[3] Over the last two decades, high-quality data of dense and continuous GPS and InSAR with a high spatial coverage and accurate measurements have revealed asymmetric patterns of interseismic velocities across major continental strike-slip faults such as the San Andreas fault [e.g., Johanson and

Bürgmann, 2005; Fialko, 2006], the North Anatolian fault [e.g., Meade *et al.*, 2002] and the Altyn Tagh fault [e.g., Zhang *et al.*, 2007]. Asymmetric patterns in deformation have been attributed to contrasts in elastic stiffness or thickness across the fault [e.g., Chéry, 2008; Le Pichon *et al.*, 2005; Fialko, 2006; Pollitz *et al.*, 2008, 2010].

[4] However, models of surface deformation associated with faulting typically assume either a simple elastic half-space rheology or a layered rheology, with an elastic layer overlying one or more viscous or viscoelastic layers [Malservisi *et al.*, 2001]. Most such models assume the same material properties for the crust and upper mantle on either side of a fault; thus, the models result in symmetric patterns of surface deformation for a vertical strike-slip fault and could not satisfy measurements across those major continental strike-slip faults [e.g., Genrich *et al.*, 2000; Zhang *et al.*, 2007; Chéry, 2008]. As a consequence, models might mis-predict fault slip rate or locking inferences on which seismic hazard assessment strongly relies.

[5] There are several ways to produce asymmetric strain across a vertical strike-slip fault: 1) Contrast in mechanical properties of elastic layers beside the fault. [e.g., McHugh and Johnston, 1977; Rybicki and Kasahara, 1977; Fialko, 2006]. 2) Contrast in thicknesses of elastic layers beside the fault [e.g., Chéry, 2008; Vaghri and Hearn, 2012]. 3) Contrast in lower crustal/mantle viscosities across the fault

¹Graduate Institute of Applied Geology, Department of Earth Science, National Central University, Zhongli, Taiwan.

²Department of Geological Sciences, Indiana University, Bloomington, Indiana, USA.

Corresponding author: W.-J. Huang, Graduate Institute of Applied Geology, Department of Earth Science, National Central University, 300 Zhongda Rd., Zhongli 32001, Taiwan. (huang22@ncu.edu.tw)

©2012. American Geophysical Union. All Rights Reserved.
0148-0227/12/2012JB009424

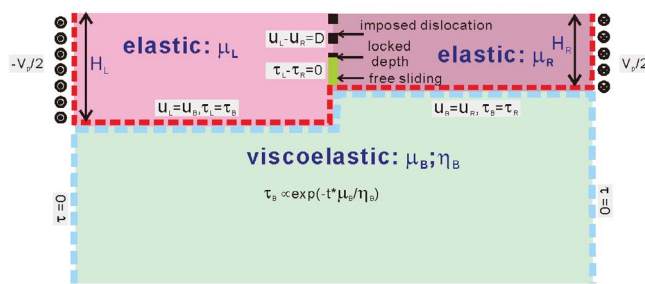


Figure 1. Setup and boundary conditions for earthquake cycle model. The dashed lines are symbolic of the discretized boundaries of three domains with different mechanical properties. Specified stress and/or displacement conditions are next to the boundaries.

[e.g., *Malservisi et al.*, 2001; *Lundgren et al.*, 2009; *Vaghri and Hearn*, 2012]. In the past decade, new schemes incorporating these considerations have been developed for analyzing asymmetry of deformation across major continental strike-slip faults. *Le Pichon et al.* [2005] modified the formulation of a screw dislocation for a fault as a bimaterial interface separating regions with different elastic moduli. They further inverted geodetic data to quantify several cases of significant asymmetry in interseismic and coseismic deformation along large continental strike-slip faults using the modified model. *Chéry* [2008] used a 1D model based on a stress balance principle to show that elastic thickness is inversely proportional to strain rate for a pure strike-slip fault. He suggested that the asymmetry of deformation across the San Andreas fault may result from elastic plate thickness variations. Several groups have used finite element models incorporating variations in stiffness and thickness of elastic layers and viscosity of viscoelastic half-spaces to analyze such asymmetric patterns of deformation [e.g., *Schmalzle et al.*, 2006; *Lundgren et al.*, 2009; *Vaghri and Hearn*, 2012]. *Pollitz et al.* [2008, 2010] utilize semi-analytical elastic moduli perturbation approaches. Furthermore, these long-lived faults could develop to be compliant zones of low elastic stiffness where the stiffness ratio of outside to inside the zone could reach to a value of approximately 2 to 3 [*Hearn and Fialko*, 2009]. Such a contrast could complicate the pattern of deformation across these faults.

[6] In this study we use boundary element methods to develop earthquake cycle models consisting of faulting in an elastic plate with possibly different thickness and stiffness on either side of the fault overlying a viscoelastic substrate as well as (optionally) a low-viscosity channel between the elastic plate and the viscoelastic substrate. We show the importance of the effect of viscous flow within the substrate, which is neglected in elastic half-space models [e.g., *d'Alessio et al.*, 2005; *Meade and Hager*, 2005] and plate models [e.g., *Chéry*, 2008; *Jolivet et al.*, 2008], and the importance of the effect of a low-viscosity channel on an asymmetric pattern of deformation. In particular, we show that the effect of a contrast in elastic properties across the fault increases with decreasing viscosity of the underlying viscoelastic lower crust/upper mantle.

[7] Although previous studies have identified contrasts in crustal properties across faults using geodetic data, these

studies have relied on either purely elastic half-space or plate models that neglect mantle flow, or finite element models that are too computationally costly to conduct complete inversions. The purpose of this paper is to develop forward boundary element models that incorporate the lateral variations in elastic properties and mantle flow at depth and are also computationally efficient. We use the boundary element models and fully probabilistic inversion methods to thoroughly investigate the range of contrasts in elastic properties across faults that are allowable by the data. We investigate asymmetric geodetic velocity profiles across the Renun segment of the Great Sumatra fault, the Carrizo segment of the San Andreas fault, and the segment of Altyn Tagh fault near Aksay at the northern border of the Tibetan plateau between the Tarim and the Qaidam basins. We use the geodetic data to infer lateral variations in crustal elastic properties (thickness/ stiffness), fault locking depths, viscosity of the lower crust/upper mantle, and average earthquake recurrence time. For the Altyn Tagh data, we investigate the resolvability of a low-viscosity lower crustal channel under the Tibetan plateau.

[8] We first describe the modeling approach and illustrate the effect of stiffness and thickness contrasts of elastic layers and a low-viscosity channel on asymmetric patterns of interseismic velocity field across a vertical strike-slip fault. Then, we analyze three cases mentioned above, compare the inversion results with previous studies and discuss the questions we addressed.

2. Earthquake Cycle Model

[9] The models in this study build on a boundary element model (BEM) first used in *Johnson et al.* [2009], which is a simple version (no cycles, just one earthquake) of these models. We extend the displacement-discontinuity boundary element method for elasticity [e.g., *Crouch and Starfield*, 1983] to incorporate linear Maxwell viscoelastic domains. Unlike the popularity of the finite element method, the BEM is less familiar to earth science researchers. Therefore, we first describe the general scheme of our models and then explain how to compute the earthquake cycles and achieve a cycle-invariant velocity profile via the boundary element technique in some detail. Finally, we examine the effects of contrasts in elastic stiffness and thickness and an embedded low-viscosity channel on the asymmetry of deformation at the ground surface.

2.1. Modeling Approach

[10] Our basic model (without a viscoelastic channel) is illustrated in Figure 1. The upper/middle crust is treated as an elastic plate overlying a viscoelastic lower crust/mantle. The elastic plate is composed of two blocks (i.e., adjoining layers) with possibly different elastic moduli and thickness separated by a vertical strike-slip fault. The model region has a finite width perpendicular to the fault (500 km on each side of the fault for this study) and an infinite length parallel to the fault. The elastic plate overlies a bottomless (linear) Maxwell viscoelastic substrate. Total relative velocity, V_o , across the domain is imposed with velocities of $V_o/2$ at the vertical edges of the elastic plates. For simplicity, a zero shear stress boundary is assumed at the edges of the viscoelastic substrate (surface velocities are not particularly sensitive to

the treatment of this boundary). The fault separating the two elastic blocks is composed of two segments. Uniform slip of amount $s = V_o T$ is imposed at regular recurrence intervals, T , on the upper segment which is locked (zero slip) between slip events. The lower segment slides freely (i.e., zero shear resistance between the two elastic blocks). We adopt an abrupt jump in thickness between the two elastic blocks. While it may be more physically plausible to have a gradual transition between the two elastic blocks, *Schmalzle et al.* [2006] showed that there is little effect on the pattern of surface strain accumulation for a range of the transition widths between 0 and 30 km. Therefore, a gradual transition between two elastic blocks is not taken into account in the model for simplicity.

[11] This model is a two-dimensional boundary value problem for inhomogeneous bodies. It contains three homogeneous domains as shown with different background colors in Figure 1. The common sections of the two boundaries define the interface between the adjoining domains. The boundary value problem is defined by the usual displacement or traction conditions along the free portions of the boundaries, as well as by continuity conditions for the displacements and tractions along the interfaces between the domains [Crouch and Starfield, 1983]. We use the displacement discontinuity method [Crouch and Starfield, 1983] in which a solution is found by dividing the boundaries into a number of straight line elements, joined end to end, represented by (uniform) dislocation surfaces in an elastic or viscoelastic half-space. For a purely elastic problem, the displacement discontinuities of all boundary elements can be found by solving a system of linear equations

$$\mathbf{b} = \mathbf{G}\mathbf{s}, \quad (1)$$

where \mathbf{b} and \mathbf{s} are vectors of boundary conditions and displacement discontinuities, respectively, and \mathbf{G} is a matrix of Green's functions, used to relate \mathbf{s} to \mathbf{b} , based on an analytical solution of a finite-width screw dislocation in a semi-infinite-space [e.g., Segall, 2010]. \mathbf{s} can be solved for as $\mathbf{s} = \mathbf{G}^{-1}\mathbf{b}$ because the \mathbf{b} and \mathbf{G} are known. The velocities at the free surface, \mathbf{v} , can be attained at the coordinates of interest via the derived \mathbf{s} and Green's functions, \mathbf{G}_s , $\mathbf{v} = \mathbf{G}_s\mathbf{s}$.

[12] This standard displacement-discontinuity boundary element method is easily extended to Maxwell viscoelastic domains. The shear stresses in an elastic anti-plane strain problem are simply scaled by the elastic shear modulus. Thus invoking the correspondence principal of viscoelasticity, the two shear stresses in the corresponding viscoelastic domain under an imposed displacement discontinuity simply decay exponentially with time, t , following the imposed dislocation [Segall, 2010]:

$$\sigma_{12} = \sigma_{12}^e * \exp(-t/t_R) \quad (2)$$

$$\sigma_{13} = \sigma_{13}^e * \exp(-t/t_R) \quad (3)$$

where σ^e is the induced instantaneous stress in an elastic half-space, and t_R is the material relaxation time which is related to viscosity, η , and shear modulus, μ , as $t_R = 2\eta/\mu$. Displacements in the screw dislocation solution are independent of elastic moduli, so the displacements in the corresponding

viscoelastic solution are independent of time [Segall, 2010]. However, because the stresses vary with time, the solved-for displacement discontinuities, \mathbf{s} , and boundary conditions, \mathbf{b} , will vary with time. We discretize the solution in time with many small increments and conduct a boundary element calculation for displacement discontinuities in each time increment. At the j th time increment, the displacement discontinuity distribution is

$$\mathbf{s}_j = \sum_{k=0}^{j-1} \mathbf{G}(t, t_R, s_1, s_2, \dots, s_{j-1})^{-1} \mathbf{b} \quad (4)$$

where the \mathbf{G} matrices are constructed exactly as for the elastic problem but with all shear stresses scaled like in equations (2) and (3). The rate of imposed displacement discontinuity is assumed to be constant over the duration of a time increment.

[13] In the model, plate motion at the edges of the elastic layer provides a steady load while coseismic rupture periodically loads the elastic plate and viscoelastic substrate. The coseismic load is relaxed at a rate determined by the relaxation time of the substrate and the elastic properties of the plate. Relaxing flow in turn reloads the elastic plates. In order to "spin up" this sequential response and attain a cycle-invariant velocity profile, we must include a sufficient number of imposed earthquake cycles, each of which is divided into an adequate number of time steps as shown in Figure 2. The number of earthquake cycles is determined according to the ratio of the upper mantle relaxation time, t_R , to recurrence time of earthquakes, T . As this ratio increases, more earthquake cycles are needed. We empirically determined that for t_R/T ratios of 0.125, 0.625, 1.25 and 2.5, we need 10, 20, 40 and 60 earthquake cycles, respectively, to sufficiently spin up the model. For models with the ratio of time since the last earthquake, t , to recurrence time of earthquakes, T , of greater than 0.25, 45 time increments are sufficient for each earthquake cycle. It takes approximately 4, 7, 19 and 35 s on a single processor desktop machine to compute these forward models with t_R/T values of 0.125, 0.625, 1.25 and 2.5, respectively.

2.2. Parameter Examination

[14] We now examine the influence of model parameters on predicted velocity profiles. The fault is fully locked at all depths (no creep) during the inter-seismic period and slips periodically during earthquakes for all models in the following examples. The earthquake recurrence interval (T) and the viscosity (η) of the substrate are specified as 250 years and 2×10^{19} Pa s, respectively. Unit relative velocity between the two adjacent elastic blocks is applied. The solid and light-toned dashed curves in Figures 3 and 4 are velocity profiles on the ground surface perpendicular to the fault trace. Their pattern varies with time (t) since last earthquake shown in Figure 3b and 4b, and with viscosity (η) of the underlying substrate shown in Figure 3c and 4c.

2.2.1. Contrast in Elastic Stiffness

[15] Figure 3a (left) shows the model setup. The shear modulus of the elastic block at left is 5 times the shear modulus of the one at right. The thickness of two elastic blocks is 20 km. The light-toned dashed velocity profiles in Figures 3b (left) and 3c (left) result from the same models but the elastic layer has a uniform shear modulus.

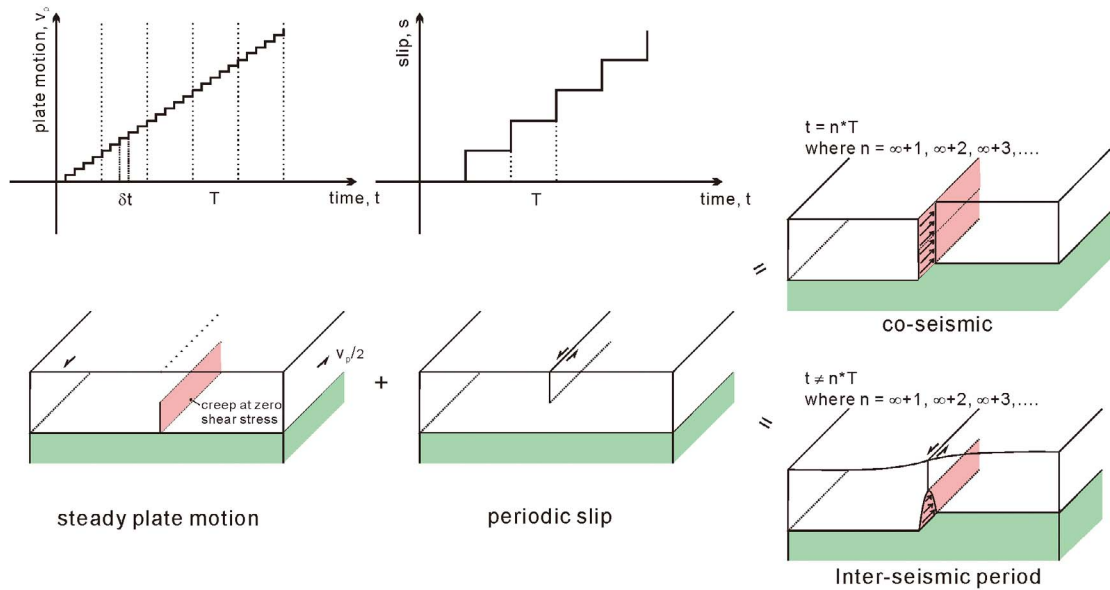


Figure 2. Illustrative scheme for computing an earthquake cycle-invariant velocity profile. T is earthquake recurrence interval.

2.2.1.1. Deformation at Various Times

[16] The solid curves in Figure 3b (left) are velocities for different times since the last earthquake: 1, 50, 100 and 200 years. The viscosity (η) of the substrate is specified as 2×10^{19} Pa s which is equivalent to a stress relaxation time ($2\eta/\mu$) of approximately 40 years. The velocities and strain rates are clearly larger on the weak side of the elastic plate (right side). The asymmetry is stronger at later times since the last earthquake.

2.2.1.2. Deformation for Various Viscosities

[17] The solid curves in Figure 3c (left) are velocities for different values of viscosity of the underlying substrate: 2×10^{18} , 2×10^{19} , 4×10^{19} , 2×10^{20} Pa s. The pronounced features are similar to curves in Figure 3b (left). The asymmetry is clearly stronger at lower viscosities.

2.2.2. Contrast in Elastic Thickness

[18] Figure 3a (right) illustrates the model setup. The thickness of the elastic block at left, 80 km, is 4 times the one at right, 20 km. The solid curves in Figure 3b (right) and 3c (right) are velocity profiles for the model with contrast in thickness. The dashed velocity profiles show model results for the case that the elastic layer has a uniform thickness of 20 km and other parameters the same.

2.2.2.1. Deformation at Various Times

[19] The solid curves in Figure 3b (right) are velocity profiles on the ground perpendicular to the fault trace for times since last earthquake: 1, 50, 100 and 200 years, respectively. The viscosity (η) of the substrate is specified as 2×10^{19} Pa s which results in a relaxation time ($2\eta/\mu$) of approximately 40 years. The influence of contrast in elastic thickness is similar to the influence of contrast in stiffness. The velocities and strain rates are again larger on the weak side of the elastic plate (right side) and the asymmetry is stronger at later times since the last earthquake. However, the influence of contrast in elastic thickness is not identical to the influence of contrast in elastic stiffness. The velocities

on the thin side of the plate (right side) in Figure 3c are very similar to the predicted velocities for the uniform thickness model and the velocities on the thick side (left side) vary less with time since the earthquake and display lower strain rates than the uniform model and the model with contrast in stiffness. The asymmetry is also more pronounced at earlier times in the model with contrast in layer thickness than the model with contrast in elastic stiffness.

2.2.2.2. Deformation for Various Viscosities

[20] The solid curves in Figure 3c (right) are velocity profiles on the ground perpendicular to the fault trace for different values of viscosity of the underlying substrate: 2×10^{18} , 2×10^{19} , 4×10^{19} , 2×10^{20} Pa s. The asymmetry is more pronounced at lower viscosity. Again, the effect of contrast in elastic thickness is not identical to the effect of contrast in elastic stiffness. The model with the elastic stiffness contrast displays appreciable asymmetry for all viscosities whereas the model with only an elastic thickness contrast does not display appreciable asymmetry at higher viscosities. We note that our results are similar to those of *Vaghri and Hearn* [2012] who constructed nearly exactly the same model using finite elements. Both models show more asymmetry for lower viscosities and late in the interseismic interval and less variation in velocity with time on the thick plate side.

2.2.3. Effect of Embedded Low-Viscosity Channel

[21] Figure 4a shows the model setup. A viscoelastic channel with low viscosity (η_1) is embedded on the right side between the elastic block and the underlying substrate. The elastic thickness on the left side is 30 km while the right side is 20 km thick. The embedded layer is 10 km thick. The viscosity (η_2) of the substrate is 2×10^{21} Pa s. The dashed lines in the background of Figures 4b and 4c are for comparison and produced with a model with the same parameters except there is no embedded low-viscosity layer (i.e., $H_R = 30$ km).

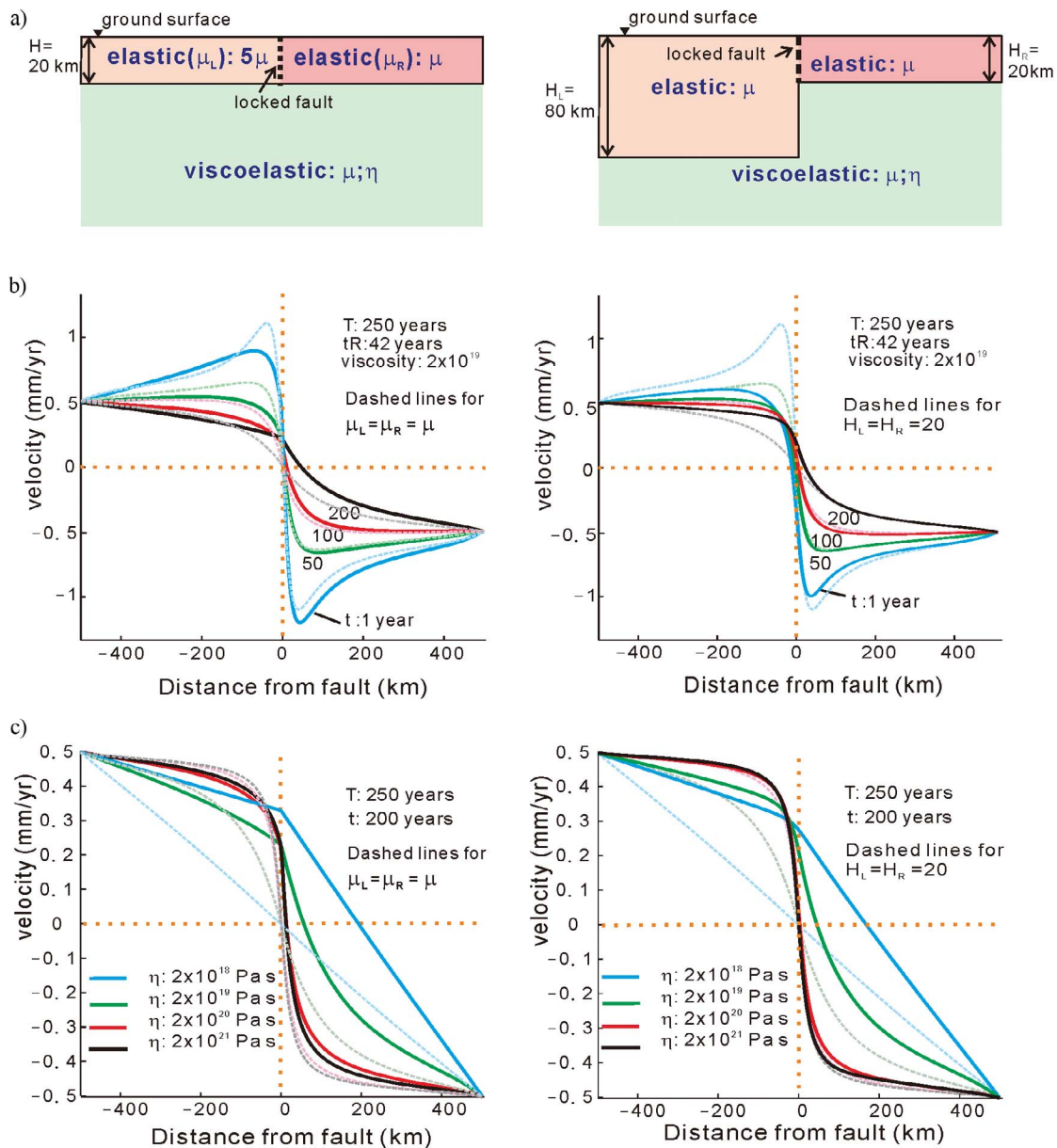


Figure 3. Velocity profiles perpendicular to fault trace from earthquake cycle models. On the left is the effect of the contrast in elastic stiffness and on the right is the effect the contrast in thickness. (a) Model setup. (b) At various times since last earthquake. (c) With various viscosities of upper mantle.

2.2.3.1. Deformation at Various Times

[22] The solid curves in Figure 4b show velocities for times since last earthquake: 1, 50, 100 and 200 years. The viscosity (η_1) of the embedded layer is 2×10^{19} Pa s. The velocity profile looks like a trough in near-fault range to the right of the fault in earlier time (i.e., small t) and then become a smooth concave in later time. Thus, the effect of the embedded low-viscosity layer on symmetry of velocity profile is discernible on the right in an earlier time (i.e., small t) but becomes minor in later times (i.e., larger t).

2.2.3.2. Deformation for Various Viscosities

[23] The solid curves in Figure 4c are velocity profiles on the ground perpendicular to the fault trace for different values of viscosity of the embedded layer (η_1), 2×10^{18} , 2×10^{19} , 2×10^{20} , 2×10^{21} Pa s. The time since last earthquake

is specified as 100 years. The velocity profile seems concave to the right of the fault trace with low viscosity (i.e., $\eta_1 = 2 \times 10^{18}$ Pa s) and then become flat with high viscosity. Thus, the effect of the embedded layer on symmetry of velocity profile is obvious with lower viscosity but becomes indistinctive with higher viscosity.

3. Inversion Scheme

[24] The efficiency of the boundary element model allows us to conduct complete inversions for the posterior probability distribution of all unknown parameters. We use a Monte Carlo-Metropolis method [e.g., *Mosegaard and Tarantola, 2002*]. We incorporate bounds on parameters by assuming box functions for priori distributions; the distributions are

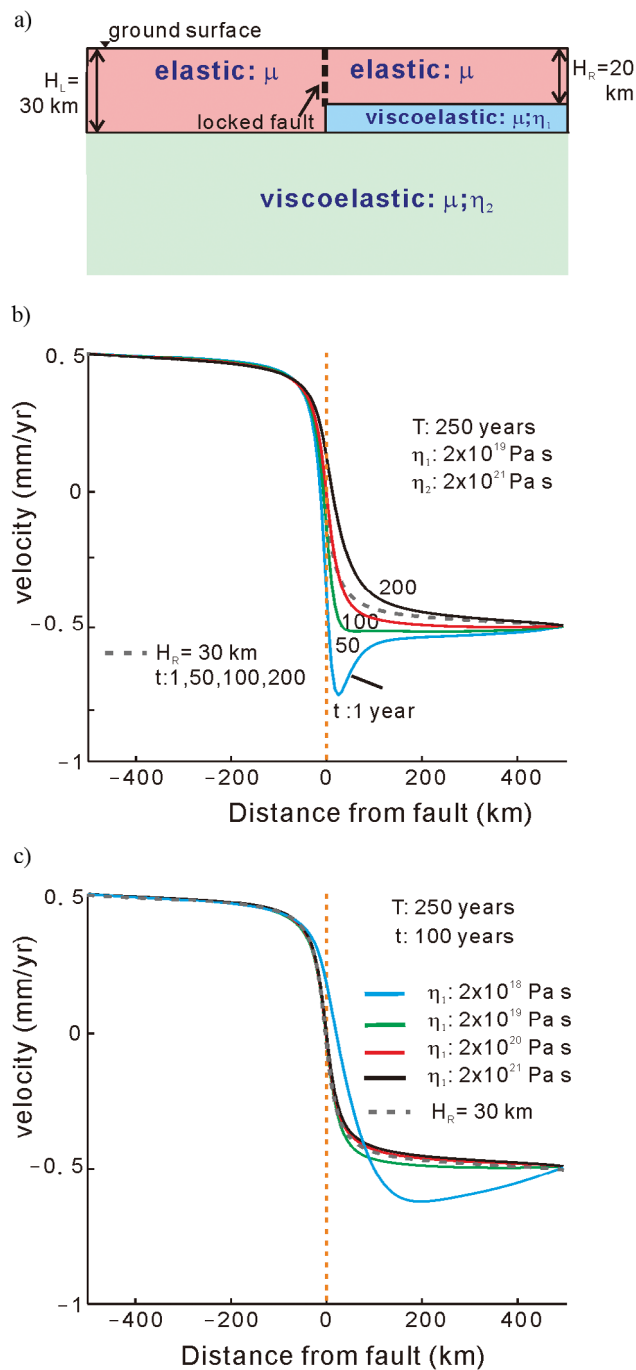


Figure 4. Velocity profiles perpendicular to fault trace with the effect of an embedded low-viscosity channel from earthquake cycle models. (a) Model setup. (b) At various times since last earthquake. (c) With various viscosities of lower crust.

constant within the bounds listed in Tables 1, 3 and 5, and zero outside the bounds. For parameters without bounds, we assume uniform prior distributions. To sample the posterior distribution, we initiate a random walk through the model space that samples the a priori distribution. The random walk is a so-called Markov Chain random walk in which the probability of visiting the model m_j , given that the current model is m_i , depends only on m_i and not on previously

visited models, where m is the vector of model parameters. The model m_j , with d unknowns, is generated randomly from m_i as follows:

$$m_j = m_i + \sum_{k=1}^d \alpha_k \gamma_k e_k \quad (5)$$

where γ_k is a $(-1, 1)$ uniform random deviate, e_k is the unit vector along the k th axis in parameter space, and α_k scales the step size along coordinate directions and is determined empirically. To sample the a posteriori distribution, this random walk is directed with a so-called Metropolis step. The random walk does not automatically move from m_i to m_j . The walk moves to the next model with probability

$$P_{ij} = \min\left(1, \frac{\rho_D(g(m_j))}{\rho_D(g(m_i))}\right). \quad (6)$$

[25] If the model m_j is not accepted, a new random step is generated from m_i . ρ_D is the probability density function of the model parameters given only the information from the data [Mosegaard and Tarantola, 2002]. For more description and discussion about this inversion scheme refer to Fukuda and Johnson [2008].

4. Analysis Using Earthquake Cycle Models

4.1. Great Sumatra Fault Near Lake Toba, Indonesia

4.1.1. Geological Setting and Ground Deformation

[26] The Great Sumatra fault belongs to a class of trench-parallel strike-slip fault systems and works in concert with

Table 1. A Priori Bounds for Renun Segment of GSF

Parameter	Symbol	Minimum	Maximum
Renun segment of GSF fault slip rate, ^a mm/yr	\dot{S}	23	27
Elastic thickness of B_{NE} , ^b km	H_{NE}	20	70
Elastic thickness of B_{SW} , ^b km	H_{SW}	20	70
Logarithmic stiffness ratio of B_{NE} to B_{SW} (rigidity ratio) ^c	R_{lr} (R_r)	-1.2	1.2
Renun segment of GSF fault recurrence interval, ^d years	T	88	240
Half-space relaxation time, ^e years	t_R	0	240
Locking depth, km	D	0	70
Time since 1921 earthquake, ^{e,f} years	t	88	88 (fixed)

^aSieh et al. [1991] and [Sieh and Natawidjaja, 2000] estimated the value of long-term fault slip as 27 mm/yr. McCaffrey et al. [2000] found arc-parallel velocities of 23~27 mm/yr for the northern Sumatra region.

^bPollitz et al. [2006] adopted an elastic layer 62 km thick in their model. We extend it to a range of 20 to 70 km. B_{NE} : block northeast of Renun segment of GSF; B_{SW} : block southwest of Renun segment of GSF.

^cLe Pichon et al. [2005] indicated that the typical range of average values of the elastic parameter is an order of magnitude from mantle to sediment (e.g., from peridotite ($14\sim 16 \times 10^{10}$ Pa) to shale ($1\sim 3 \times 10^{10}$ Pa)), and the ratio is unlikely to exceed an order of magnitude anywhere.

^dBellier and Sebrier [1995] inferred a northward increase of hazard along the SFS (Sumatra fault system) with recurrence intervals of 400 ± 200 years for a maximum expected $M_w = 7.2$ event in southern Sumatra and of 160 ± 80 years for a $M_w = 7.7$ maximum expected earthquake at $2^\circ N$.

^eMaximum bound of t_R is specified as same as maximum bound of T because t_R of larger than the maximum bound is irresolvable.

^fSieh and Natawidjaja [2000] reported the Renun segment (i.e., the segment of GSF in this region) the source of three major earthquakes early in the twentieth century. The possible biggest one occurred on April 1, 1921.

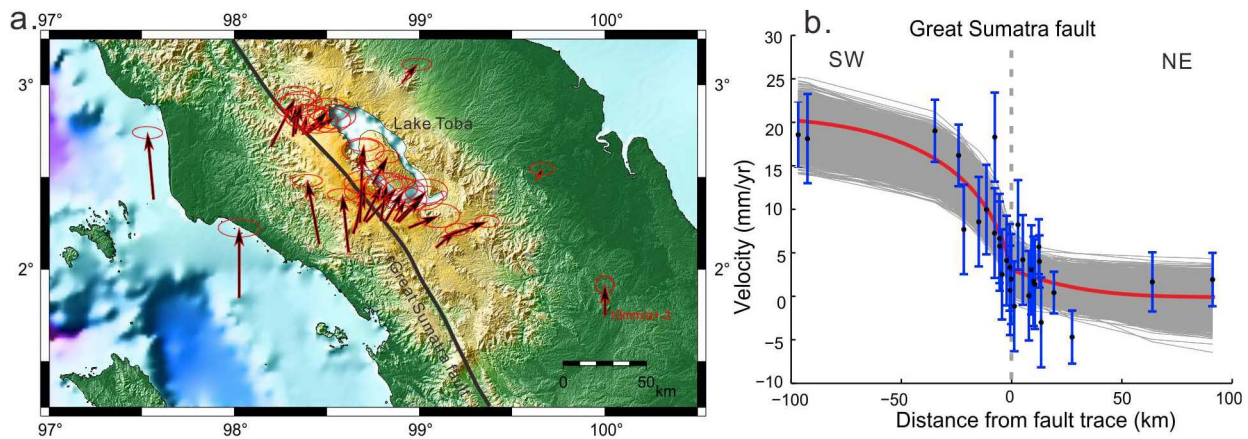


Figure 5. (a) GPS observations along Dolok Sanggul transects west of Lake Toba (published by *Genrich et al.* [2000]). (b) Projection of fault-parallel components of the GPS velocities along profile perpendicular to Great Sumatra fault. Error bars are σ . Grey lines are sampled fits and red line is average fit from inversion.

the Sumatran subduction zone to accommodate obliquely convergent plate motion between Australian/Indian and Eurasia plates [*Yeats et al.*, 1997; *Sieh and Natawidjaja*, 2000]. The part of the Great Sumatra fault (GSF), named Renun segment [*Aldiss et al.*, 1983], runs along the western flank of the 80-km-long caldera on which center Lake Toba is situated. The Lake Toba is situated in the center of the caldera. The segment traverses the thick pyroclastic flow deposit erupted 73,000 years ago. *Sieh et al.* [1991] and *Sieh and Natawidjaja* [2000] estimated the value of long-term fault slip as 27 mm/yr. *McCaffrey et al.* [2000] found arc-parallel velocities of 23~27 mm/yr for the northern Sumatra region. The GPS observations along the Sidikalang transect and Dolok-Sanggul transect west of lake Toba published by *Genrich et al.* [2000] is an excellent example of asymmetry in interseismic deformation. Figure 5a shows the GPS velocities along the Dolok Sanggul transect and Figure 5b is the projection of the fault-parallel components of the observed velocities along the profile perpendicular to the fault. The observed velocities southwest of the Great Sumatra fault range from almost zero near the fault to up to 20 mm/yr away from it. In contrast, almost all the measurements northeast of the fault are not significantly different from zero. The fault-normal components of the observed velocities are assumed to be attributed to the coupling on the Sumatran subduction interface [e.g., *Le Pichon et al.*, 2005]. *Genrich et al.* [2000] modeled the Renun segment as a vertical strike-slip fault in an elastic half-space. In order to fit well the asymmetric deformation pattern, the locations of their modeled fault planes were shifted 14 ± 3 km west of the trace for the Dolok Sanggul transect and 24 ± 4 km west of the trace for the Sidikalang transect. *Le Pichon et al.* [2005] estimated the contrast in stiffness ratio as about 30 along the Renun segment assuming a bimaterial fault model and concluded this result is not impossible if the Toba caldera is underlain by a plug of intrusive massive rocks adjacent to a thick pile of tuffs and sediment.

4.1.2. Modeling and Inversion Results

[27] We model the 1989–1996 GPS data in the region near Lake Toba with the episodic earthquake cycle model discussed

above (Figure 1). The timing of last earthquake is constrained by an earthquake in 1921. The earthquake is the largest one among three occurred in this region in the twentieth century. It ruptured the Renun segment of GSF [*Sieh and Natawidjaja*, 2000]. Other parameters are constrained by geological and/or geophysical data as listed in Table 1.

[28] The results of the inversion are summarized in Table 2 and Figure 6 and the fit to the data is shown in Figure 5b. The fault slip rate and the thicknesses of the northeastern elastic block and the southwestern elastic block are not well resolved (Figure 7). The logarithmic stiffness ratio of B_{NE} to B_{SW} ranges from 0.34~1.15 where B_{SW} is the block southwest of Renun segment of GSF and B_{NE} is the block northeast of Renun segment of GSF; that is, the stiffness of B_{NE} is as 2.2~14.1 times larger than the one of B_{SW} . The Renun segment of GSF recurrence interval is in the range of 101.5~237.6 years. The relaxation time of mantle in this region is in the range of 20.5~208.5 years. In terms of viscosity, it ranges from 1.0 to 10.0×10^{19} Pa s. The locking depth is in the range of 4.1~25.7 km with the most likely value of 8.8 km.

4.2. San Andreas Fault in Carrizo Plain, USA

4.2.1. Geological Setting and Ground Deformation

[29] The Carrizo segment of the San Andreas fault (SAF) lies north of the big bend region in central California (Figure 8). It separates Franciscan assemblages northeast of the fault from the Salinian block to the southwest. Franciscan

Table 2. Renun Segment of GSF Inversion Results

Parameter	A Priori Bounds	95% Confidence	Most Probable
\dot{S} , mm/yr	23~27	23.2~26.8	none (almost uniform)
H_{NE} , km	20~70	22.8~67.6	none (almost uniform)
H_{SW} , km	20~70	22.7~67.1	none (almost uniform)
R_{fr}	-1.2~1.2	0.34~1.15	0.78
T , years	88~240	101.5~237.6	238.5
t_R , years	0~240	20.5~208.5	84
D , km	0~70	4.1~25.7	8.8

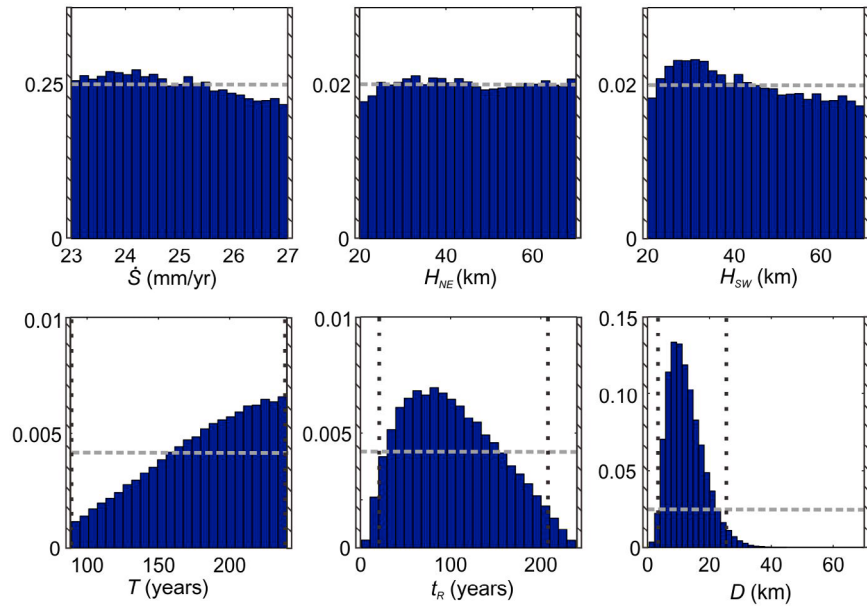


Figure 6. Probability histograms of parameters for Renun segment of Great Sumatra Fault inversion. \dot{S} is Carrizo segment of SAF fault slip rate. H_{NE} is thickness of northeastern elastic block. H_{SW} is thickness of southwestern elastic block. T is Carrizo segment of SAF fault recurrence interval. t_r is half-space relaxation time. Hatched lines show a priori bounds. Dashed lines show a priori distributions.

assemblages are interpreted as a former subduction zone complex which includes both oceanic and terrigenous materials [Page, 1981]. The assemblages contain sedimentary rocks and tectonic mélanges. In contrast, the Salinian block is interpreted as part of a former magmatic arc and is composed

mostly of igneous rocks and metamorphic rocks [Page, 1981].

[30] An average slip rate of 33.9 ± 2.9 mm/yr for the past 3,700 years and $35.8 + 5.4/-4.1$ mm/yr for the past 13,250 years were determined by Sieh and Jahns [1984]

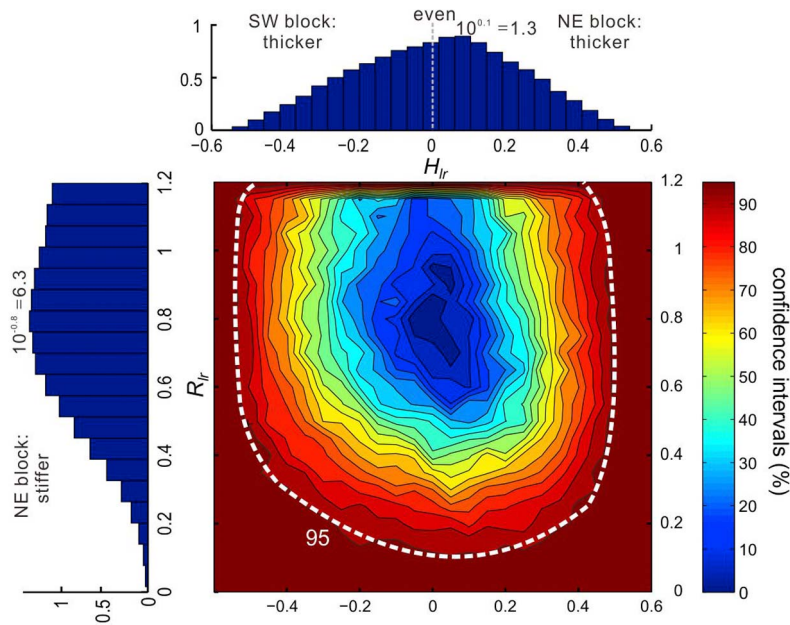


Figure 7. Probability of logarithmic thickness ratio versus stiffness ratio for Renun segment of Great Sumatra fault inversion. H_{lr} is logarithmic thickness ratio of northeastern elastic block to southwestern elastic block. R_{lr} is logarithmic stiffness ratio of northeastern elastic block to southwestern elastic block. Dotted lines show 95% confidence intervals.

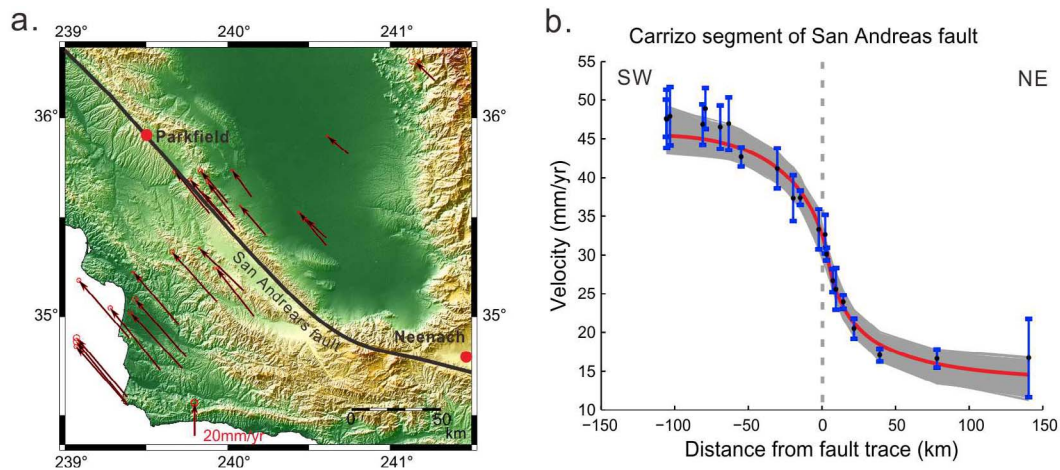


Figure 8. (a) GPS velocities in Carrizo Plain region of southern California. (b) Projection of fault-parallel components of GPS velocities onto profile perpendicular to San Andreas fault. Error bars are 2σ . Grey lines are sampled fits and red line is average fit from inversion.

based on the studies of the evolution of a channel, related landforms, deposits and excavations in the region of Wallace creek. *Liu-Zeng et al.* [2006] studied three dimensional excavations across the San Andreas fault at Wallace Creek and attained a similar slip rate of 34 ± 3 mm/yr for the period of A.D. 1210 to A.D. 1857. The geodetic determination of strain accumulation also resulted in a similar range of 31 to 35 mm/yr over a 175 km aperture spanning the fault [e.g., *Lisowski et al.*, 1991; *Feigl et al.*, 1993]. *Lisowski et al.* [1991] pointed out that the profile of the $N43^\circ W$ velocity component for their Carrizo network is asymmetric and suggested two possible explanations for the asymmetry: one is due to the proximity of the Carrizo network to the western corner of the big bend in the San Andreas fault and the other is due to the effects of lateral inhomogeneity of elastic properties. Figure 8a shows the distribution of horizontal 1994~2003 GPS velocities and Figure 8b shows the projection of fault-parallel components of the velocities onto the profile perpendicular to the San Andreas fault. Apparently, the velocities are dominated by the fault-parallel

components and the strain accumulation is similar to those from previous geodetic studies. *Schmalzle et al.* [2006] used these GPS data to characterize asymmetric surface deformation across the Carrizo segment and interpreted those data in terms of lateral variation of elastic properties of upper crustal rocks. *Fulton et al.* [2010] found a 20 km wide compliant zone northeast of the Carrizo segment requires an extremely low value of Young's modulus in order to explain the same GPS data.

4.2.2. Modeling and Inversion Results

[31] We model the 1994–2003 GPS data in the Carrizo plain of the San Andreas fault system analyzed and collected by *Schmalzle et al.* [2006] with the episodic earthquake cycle model discussed above (Figure 1). The timing of the last earthquake is constrained by the Fort Tejon earthquake in 1857 caused by rupture of the San Andreas fault from near Parkfield to near San Bernardino (160 km southeast of Neenach in Figure 8a), with fault slip of up to 9.5 m [*Agnew and Sieh*, 1978]. Other parameters are constrained by geological and/or geophysical data listed in Table 3. The results of the inversion are summarized in Table 4 and Figure 9 and the fit to the data is shown in Figure 8b. The estimated range of fault slip rate is not significantly refined from the geologic range, but the inversion favors higher slip rates of 35.5–37.0 mm/yr. The thickness of the northeastern elastic block (B_{NE} , Franciscan assemblages) ranges from 20.2 to 49.3 km and the thickness of the southwestern elastic block (B_{SW} , Salinian block) ranges from 14.3 to 48.3 km. However, the logarithmic thickness ratio of B_{NE} to B_{SW} ranges from -0.25 to 0.44 ; that is, a thickness contrast cannot be resolved. The

Table 3. A Priori Bounds for Carrizo Segment of SAF

Parameter	Symbol	Minimum	Maximum
Carrizo segment of SAF fault slip rate, ^a mm/yr	\dot{S}	31	37
Elastic thickness of B_{NE} , ^b km	H_{NE}	10	50
Elastic thickness of B_{SW} , ^b km	H_{SW}	10	50
Logarithmic stiffness ratio of B_{NE} to B_{SW} (rigidity ratio)	R_{lr}	none	none
Carrizo segment of SAF fault recurrence interval, ^c years	T	146	415
Half-space relaxation time, ^d years	t_R	0	415
Locking depth, km	D	0	50
Time since 1857 earthquake, ^e years	t	146	146 (fixed)

^a*Sieh and Jahns* [1984]; *Jackson et al.* [1995]; *Liu et al.* [2004]; *Liu-Zeng et al.* [2006].

^b B_{SW} : block southwest of Carrizo segment of SAF; B_{NE} : block northeast of Carrizo segment of SAF.

^c*Field et al.* [2008].

^dMaximum bound of t_R is specified as same as maximum bound of T because t_R of larger than the maximum bound is irresolvable.

^e*Agnew and Sieh* [1978].

Table 4. Carrizo Segment of SAF Inversion Results

Parameter	A Priori Bounds	95% Confidence	Most Probable
\dot{S} , mm/yr	31~37	31.5~36.9	35.3
H_{NE} , km	10~50	20.2~49.3	45.8
H_{SW} , km	10~50	14.3~48.3	20.0
R_{lr}	None	$-0.37 \sim -0.01$	-0.09
T , years	146~415	220~412	413
t_R , years	0~415	12~358	20
D , km	0~50	10.0~22.9	15.5

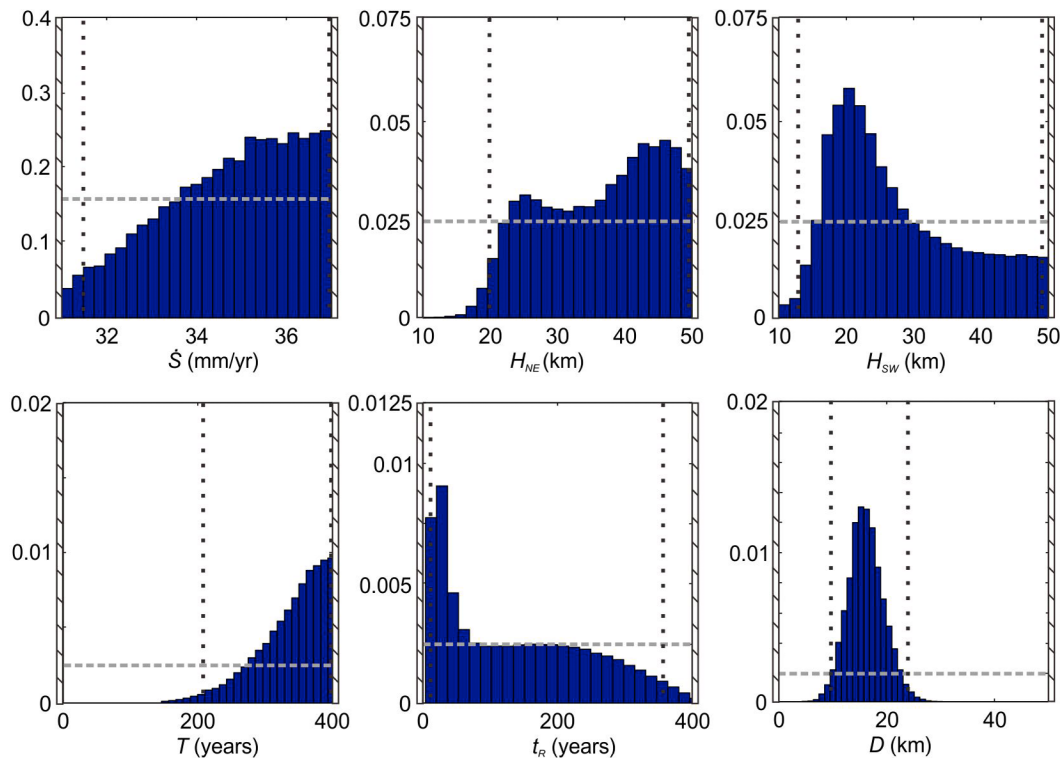


Figure 9. Probability histograms of parameters for Carrizo segment of SAF inversion. \dot{S} is Carrizo segment of SAF fault slip rate. H_{NE} is thickness of northeastern elastic block. H_{SW} is thickness of southwestern elastic block. T is Carrizo segment of SAF fault recurrence interval. t_r is half-space relaxation time. Dotted lines show 95% confidence intervals. Hatched lines show a priori bounds. Dashed lines show a priori distributions.

logarithmic stiffness ratio of B_{NE} to B_{SW} ranges from -0.37 to -0.01 ; that is, the stiffness of B_{SW} is 1.0–2.3 times larger than that of B_{NE} . Figure 10 shows a plot of the probability of logarithmic thickness ratio versus probability of logarithmic stiffness ratio. The Carrizo segment of SAF recurrence interval is in the range of 220–412 years. The relaxation time of the mantle in this region is in the range of 12–358 years. In term of viscosity, it ranges from 5.7×10^{18} to 1.7×10^{20} Pa s. The locking depth is in a range of 10.0–22.9 km with a most likely value of 15.5 km.

4.3. Altyn Tagh Fault in the Aksay Region, China

4.3.1. Geological Setting and Ground Deformation

[32] The 2500-km-long Altyn Tagh fault (ATF) system along the northern border of the Tibetan plateau accommodates sinistral (left-lateral) motion between the Tarim basin to the north and the Qaidam basin to the south (Figure 11) within the India-Eurasia collision zone [Tapponnier and Molnar, 1977; Washburn *et al.*, 2001]. The characteristics of the ATF system vary along its trend in terms of its geometric appearance, displacement and slip rate [Peltzer *et al.*, 1989; Ge *et al.*, 1992; Meyer *et al.*, 1996; Van der Woerd *et al.*, 2001; Mériaux *et al.*, 2004, 2005]. In our study region (longitude $\sim 93^\circ\text{E}$ to $\sim 95^\circ\text{E}$ and latitude $\sim 37.5^\circ\text{N}$ to $\sim 41.5^\circ\text{N}$) the ATF system comprises two principle parallel strands. The northern branch (NATF) is the more recent Quaternary fault while the southern branch (SATF) is described as the primary fault in terms of cumulative motion over longer time scales [Mériaux *et al.*, 2005; Jolivet *et al.*, 2008]. The two branches are active. The parts of NATF and SATF in our study

area are approximately equivalent to Aksay segment and Dangjin-Shankou segment, respectively, named by Mériaux *et al.* [2005]. Mériaux *et al.* [2005] suggested that a great earthquake ($M > 8$) could have ruptured the segments west of Aksay segment and Dangjin-Shankou segment on NATF and SATF in the last few hundred years but the Aksay segment and Dangjin-Shankou segment would have been quiescent for longer. They estimated a 17.8 ± 3.6 mm/yr Holocene slip rate on the Aksay segment of NATF near Bang Gou Ba site (94.81°N , 39.50°N) consistent with the estimates of Van der Woerd *et al.* [2001] at Subei farther to the east ($\sim 94.9^\circ\text{N}$, $\sim 39.4^\circ\text{N}$). This rate is significantly faster than the late Quaternary slip rate of 10 ± 2.5 mm/yr of the Aksay segment obtained by Zhang *et al.* [2007] near Huermo Bulak, (94.47°E , 39.42°N). No report about fault slip of the Dangjin-Shankou segment of SATF is found. The current leading front of the India-Eurasia collision zone is likely the NATF in our study region.

[33] InSAR data covering the 1995–2006 period shows distinct asymmetry of interseismic velocity distribution around longitude 94°E (Figure 11) [Lasserre *et al.*, 2007; Jolivet *et al.*, 2008]. This asymmetry is also observed in GPS measurements. The GPS measurements spanning the fault between 93°E and 95°E show a mean velocity of -0.7 ± 1.5 mm/yr in the Tarim basin cluster and the upper bound velocity of 8.1 ± 1.7 mm/yr in the Qaidam basin [Zhang *et al.*, 2007].

4.3.2. Modeling and Inversion Results

[34] We model the interferometric synthetic aperture radar (InSAR) data across the ATF system around longitude 94°E

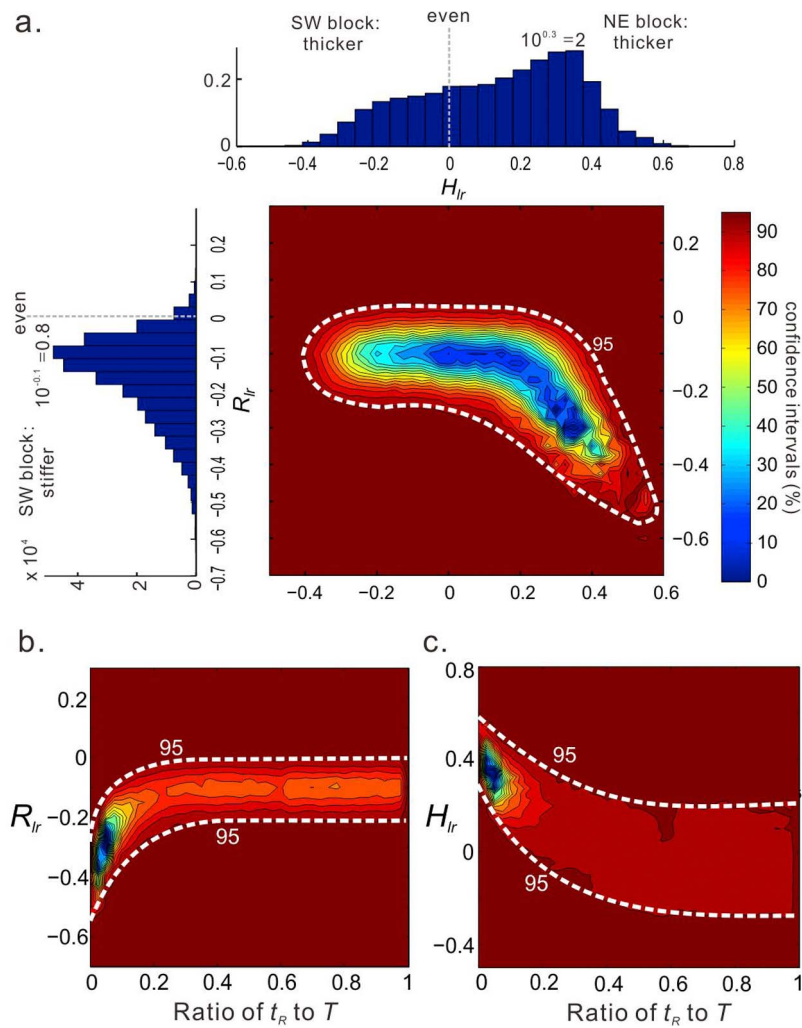


Figure 10. (a) Probability of logarithmic thickness ratio versus probability of logarithmic stiffness ratio for Carrizo segment of San Andreas fault inversion. H_{lr} is logarithmic thickness ratio of northeastern elastic block to southwestern elastic block. R_{lr} is logarithmic stiffness ratio of northeastern elastic block to southwestern elastic block. (b) Probability of logarithmic stiffness ratio versus probability of ratio of t_R to T . t_R is half-space relaxation time. T is Carrizo segment of SAF fault recurrence interval. (c) Probability of logarithmic thickness ratio versus probability of ratio of t_R to T .

covering the 1995–2006 period [Lasserre *et al.*, 2007] with a modified episodic earthquake cycle model as shown in Figure 4a. We didn't directly use all the InSAR data shown in Figure 11a; instead, we only use fault-parallel horizontal component of the data and attained a moving average along the profile perpendicular to the fault (Figure 11b). There is an additional semi-infinite viscoelastic layer embedded between the elastic block to the right of the fault and viscoelastic half-space substrate as shown in Figure 4. This modified model enables us to examine the existence of a low-viscosity mid crust underneath the Tibetan plateau and estimate its viscosity. Unlike the two previous cases, t , time since last earthquake, is also estimated in the inversion because of the lack of quantitative evidence for the most recent earthquake. Because there was no large earthquake around this region within the 100 year historical record, the lower bound of t is placed at 100 years. Although the ATF has two strands in this region, we assume the deformation is

attributed to NATF and ignore the possible contribution from SATF based on the studies of slip rate [Mériaux *et al.*, 2004, 2005]. Other parameters are constrained by geological and/or geophysical data listed in Table 5.

[35] The results of the inversion are summarized in Table 6 and Figure 12 and the fit to the data is shown in Figure 11b. The fault slip rate ranges from 9.8 to 13.4 mm/yr and is comparable with the late Quaternary slip rate of 10 ± 2.5 mm/yr obtained by Zhang *et al.* [2007] based on their geological studies. The rate is faster than the slip rates of 8 to 10 mm/yr from a thin plate model [Jolivet *et al.*, 2008] of InSAR data. The thickness of the northern elastic block ranges from 17.9 to 68.1 km and the southern elastic block ranges from 14.8 to 19.8 km. The logarithmic thickness ratio of B_N to B_S ranges from 0.04 to 0.60 (Figure 13); that is, the thickness of B_N (Tarim) is 1.1–4.0 times larger than that of B_S (Qaidam). The logarithmic stiffness ratio of B_N to B_S ranges from 1.06 to 1.20; that is, the stiffness of B_N (Tarim) is 11.5–15.7 times

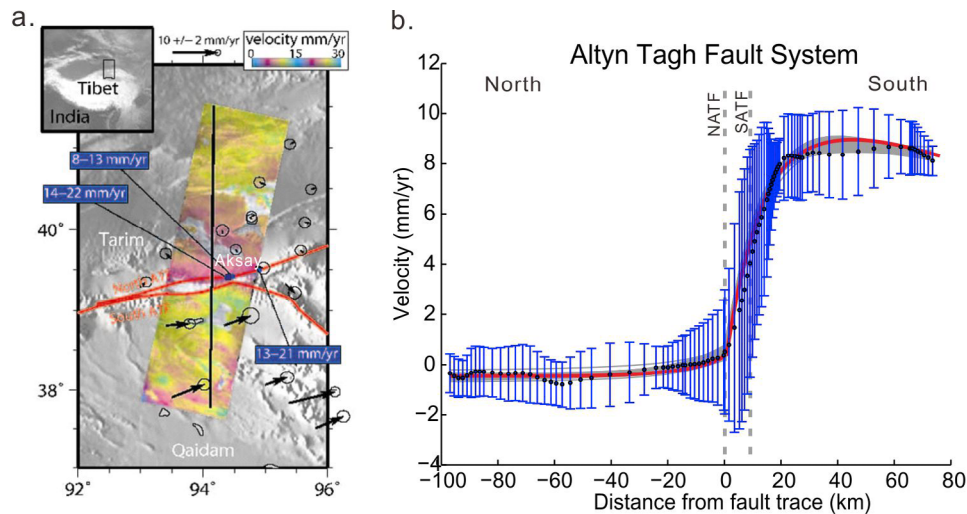


Figure 11. (a) Surface velocities across Altyn Tagh fault system in Aksay Region. Surface velocity (projected in fault-parallel direction) is shown as colored area obtained from a stack of 15 interferograms using ERS and ENVISAT radar data covering the 1995~2006 period [Lasserre *et al.*, 2007]. Estimates of the slip rate during the Holocene along the Altyn Tagh fault are given in blue boxes [Van der Woerd *et al.*, 2001; Mériaux *et al.*, 2005; Zhang *et al.*, 2007]. GPS velocities are represented as black arrows [Zhang *et al.*, 2007]. This figure is adapted from Jolivet *et al.* [2008]. (b) Projection of the velocities. Error bars are 2σ . Grey lines are sampled fits and red line is average fit from inversion result.

larger than that of B_S (Qaidam). Jolivet *et al.* [2008] attained a similar result that Tarim is stiffer than Qaidam but their stiffness ratio of northern block (Tarim) to southern block (Qaidam) does not exceed 9. The Altyn Tagh fault recurrence interval is in the range of 572~1376 years. The relaxation time of mantle in this region is in the range of 167~1418 years. In terms of viscosity, it ranges from 0.8 to 6.7×10^{20} Pa s. The locking depth is in a range of 13.0~18.7 km with a most likely value of 15.9 km. The viscosity of the mid-crustal Tibetan channel is not resolvable.

Table 5. A Priori Bounds for Altyn Tagh Fault Near Aksay

Parameter	Symbol	Minimum	Maximum
ATF fault slip rate, ^a mm/yr	\dot{S}	2	20.4
Elastic thickness of B_N , ^b km	H_N	10	70
Elastic thickness of B_S , ^b km	H_S	10	70
Logarithmic stiffness ratio of B_N to B_S (rigidity ratio) ^c	$R_{lr} (R_r)$	-1.2	1.2
ATF fault recurrence interval, ^d years	T	300	1400
Mantle relaxation time, ^d years	t_{Rm}	none	None
Locking depth, km	D	>0	70
Time since last earthquake, ^e years	t	100	none
Lower-crust relaxation time, years	t_{Rlc}	>0	1400
Thickness of lower-crust, km	H_{lc}	10	10 (fixed)

^aMériaux *et al.* [2005] estimated an average Holocene rate of 17.8 ± 3.6 mm/yr; Meyer *et al.* [1996] attained slip rate of 4 ± 2 mm/yr for the easternmost of the ATF, east of $96^\circ E$.

^b B_N : block northeast of ATF; B_S : block southwest of ATF.

^cLe Pichon *et al.* [2005] indicated that the typical range of average values of the elastic parameter is an order of magnitude from mantle to sediment, (e.g., from peridotite ($14 \sim 16 \times 10^{10}$ Pa) to shale ($1 \sim 3 \times 10^{10}$ Pa) and the ratio is unlikely to exceed an order of magnitude anywhere.

^dWashburn *et al.* [2001] attained recurrence intervals of 0.7 ± 0.4 k.y. and 1.1 ± 0.3 k.y.

^eThere was no larger earthquake around this region within 100 years in the historical record.

[36] Jolivet *et al.* [2008] applied a thin-plate model sheared at its base to the same data set and attained a locking depth of 7~9 km and a present-day geodetic slip rate of 8~10 mm/yr. They interpret the asymmetric pattern as the joint effect of a stiffness decrease from the Tarim basin to the Qaidam basin.

5. Discussion

[37] The asymmetric strain accumulation at the ground surface is attributed to stiffness and thickness contrasts across the two elastic layers (blocks) beside the fault along with an embedded low-viscosity channel (only for Altyn Tagh fault case). Our inversion results for the stiffness and thickness contrasts are listed in Table 7. Evidently, the asymmetric patterns of deformation cannot be explained for the Renun segment and the Aksay segment without unambiguous stiffness contrast (Figures 7 and 13). But, uniform thickness and stiffness cannot be ruled out for the Carrizo segment (Figure 10).

[38] For the Renun segment, the inversion result attains a range of 2.2 to 14.1 for the stiffness ratio of the northeastern

Table 6. Altyn Tagh Fault Inversion Results Without Varying Fault Zone Position

Parameter	A Priori Bounds	95% Confidence	Most Probable
\dot{S} , mm/yr	2~20.4	9.8~13.4	11.6
H_N , km	10~70	17.9~68.1	23.5
H_S , km	10~70	14.8~19.8	17.0
$R_{lr} (R_r)$	-1.2~1.2	1.06~1.2	1.18
T , years	300~1400	572~1376	925
t_{Rm} , years	none	167~1418	430
D , km	0~70	13.0~18.7	15.9
t , years	>100	119~1106	225
t_{Rlc} , years	0~1400	32~1369	None (almost uniform)

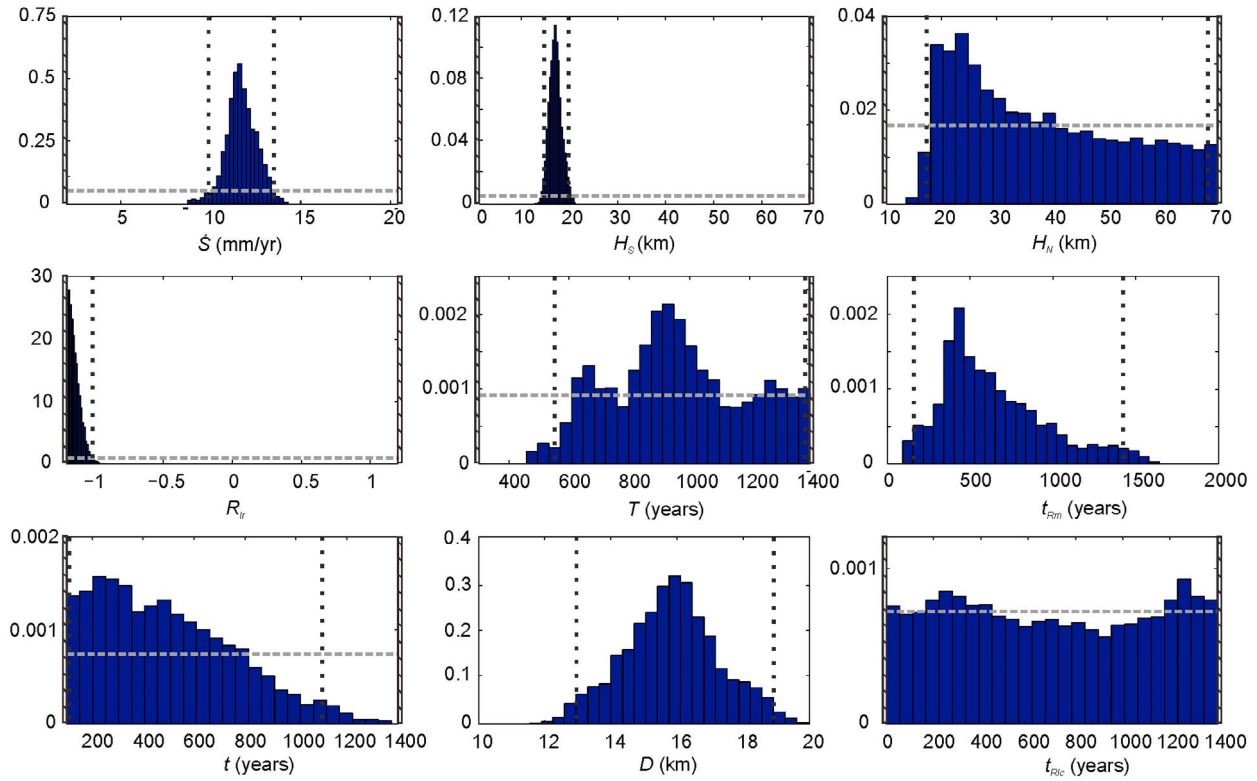


Figure 12. Probability histogram of parameters for Altyn Tagh fault inversion. \dot{S} is fault slip rate. H_S is thickness of southern elastic block. H_N is thickness of northern elastic block. R_{lr} is logarithmic stiffness ratio of southern block to northern block. t_{Rm} is mantle relaxation time. t is time since last earthquake. D is locking depth. t_{Rlc} is mid-crust relaxation time Dotted lines show 95% confidence intervals. Hatched lines show a priori bounds. Dashed lines show a priori distributions.

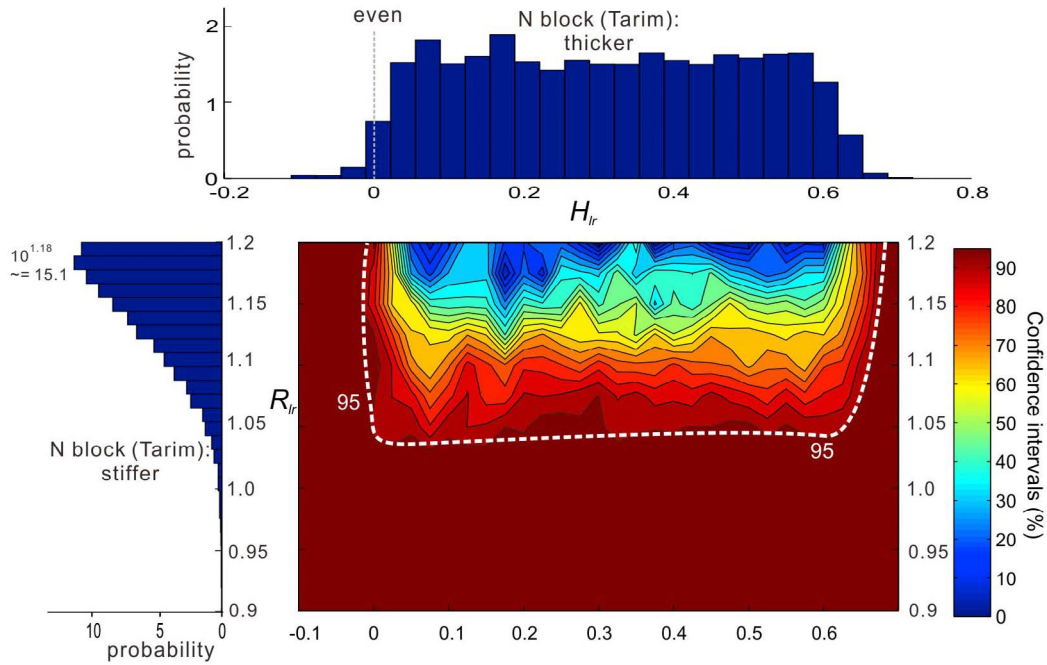


Figure 13. Probability of logarithmic thickness ratio versus probability of logarithmic stiffness ratio for Altyn Tagh fault inversion. H_{lr} is logarithmic thickness ratio of northeastern elastic block to southwestern elastic block. R_{lr} is logarithmic stiffness ratio of northeastern elastic block to southwestern elastic block.

Table 7. Inversion Results for Stiffness and Thickness Ratios of Elastic Layers

Contrast	Great Sumatra Fault		San Andreas Fault		Altyn Tagh Fault	
	95% Confidence	Most Probable	95% Confidence	Most Probable	95% Confidence	Most Probable
stiffness ratio of $B_{N(E)}$ to $B_{S(W)}$	2.19~14.13	6.03	0.43~0.97	0.81	10.51~15.68	15.25
stiffness ratio of $B_{S(W)}$ to $B_{N(E)}$	0.07~0.45	0.17	1.03~2.34	1.23	0.06~0.09	0.07
thickness ratio of $B_{N(E)}$ to $B_{S(W)}$	0.44~2.33	1.26	0.56~2.75	2.18	1.10~3.96	none
thickness ratio of $B_{S(W)}$ to $B_{N(E)}$	0.43~2.29	0.79	0.36~2.00	0.46	0.25~0.91	none

elastic layer to southwestern elastic layer and favors 6.0. This result is much smaller than the stiffness ratio of ~ 28 attained by *Le Pichon et al.* [2005] using a modified screw dislocation for a bimaterial fault (elastic half-space). It is understandable that an elastic half-space model would predict higher stiffness ratios than the plate models with relaxing flow at depth. As illustrated in Figure 3, the asymmetry in surface deformation is enhanced with decreasing viscosity in the mantle and with time elapsed since the last earthquake. Thus elastic half-space models that neglect mantle flow may significantly overpredict the contrast in elastic moduli if in reality the mantle viscosity is low enough to allow for significant amounts of relaxing flow during the earthquake cycle. The inversion result also shows that a thickness contrast alone is not able to explain the asymmetric strain accumulation across the Renun segment as the thickness of the elastic layer at either side cannot be resolved.

[39] Our estimate of stiffness contrast of 2–14 is consistent with the argument proposed by *Le Pichon et al.* [2005] that a stiffness contrast could be attributed to a plug of intrusive massive rock underneath Toba caldera adjacent to a thick pile of tuffs and sediment. *Le Pichon et al.* [2005] proposed that a stiffness ratio of up to 16 is possible assuming a Young's modulus for weak shale of $\sim 1 \times 10^{10}$ Pa and a Young's modulus for rigid peridotite of 16×10^{10} Pa. Our result suggests the additional special causes for stiffness contrast proposed by *Le Pichon et al.* [2005] (for example, the presence of gauges, hydraulic quasi-lithostatic pressure and the effect of high temperature) are not needed to explain the observed asymmetry in deformation. It remains unclear how large elastic moduli contrasts actually are in the crust. Laboratory studies [e.g., *Eissa and Kazi*, 1988] often show that static elastic moduli are 5–10% lower than dynamic values but scatter in the data allow elastic moduli to be as much as a factor of 10 lower than dynamic values. However, these laboratory tests are conducted on small rock samples and it is unclear how well these results scale to crustal-scale static loading.

[40] *Schmalzle et al.* [2006] analyzed the same data set across the Carrizo segment of the San Andreas fault using an earthquake cycle model of a fully locked vertical strike-slip fault and indicated that models with laterally uniform material properties but variable elastic block thickness (thinner crust northeast of the fault), and models with uniform block thickness but laterally variable mechanical properties (smaller Young's modulus northeast of the fault) fit the geodetic data across the Carrizo segment equally well. They took the regional seismicity into consideration which suggested the depth of the elastic block may actually be deeper northeast of the fault and rejected the models with a thinner elastic block northeast of the fault. However, they also suspected that the sparse regional seismicity may not be strong enough to

reach such a conclusion. Our inversion result attains a range of 1.0 to 2.3 on the stiffness ratio and a range of 0.4 to 2.0 on the thickness ratio of southwestern elastic block to northeastern elastic block. Because *Schmalzle et al.* [2006] used a more computationally expensive finite element method, they could not explore the entire parameter space. Our inversion result shows that an even broader range in thickness and stiffness ratios than determined by *Schmalzle et al.* [2006] is allowable by the data. Although our study shows that a uniform elastic stiffness cannot be ruled out by the data, we conclude that the elastic block southwest of the fault may be stiffer compared to the elastic block northeast of the fault, consistent with the study of *Schmalzle et al.* [2006]. This is also consistent with geologic observations that the Salinian block (southeast of the fault) lithology is stiffer than the lithology of the Franciscan assemblage.

[41] Although the thickness ratio across the San Andreas fault is not resolvable, our inversion tends to favor a higher elastic thickness to the NE. The combined result of the tomography studies from *Magistrale et al.* [2000], and *Zhu and Kanamori* [2000] showed that the crust is thicker to the NE of the Carrizo SAF (Moho depth of up to 40 km beneath Sierra Nevada) than to the SW (Moho depth of 24 km adjacent to SAF). *Lin et al.* [2010] showed lower P wave velocity (lower stiffness) to the NE of SAF in the upper 10 km, but the contrast in stiffness is opposite between 10 km and 20 km in depth in a NE-SW cross-section passing through Parkfield. Their result also showed the crust is very thick under the Sierra Nevada Mountains. Thus, we speculate perhaps the slight tendency for thicker elastic layer to the NE and stiffer to the SW in our results is because of the thick Sierra Nevada crust.

[42] For the Aksay segment, the inversion result attains ranges of 11.0 to 15.9 for the stiffness ratio (most likely 15.4) and 1.1 to 4.0 for the thickness ratio of B_N to B_S . This result

Table 8. Altyn Tagh Fault Inversion Results With Varying Fault Zone Position^a

Parameter	A Priori Bounds	95% Confidence	Most Probable
\dot{S} , mm/yr	2~20.4	9.1~10.8	10.1
H_N , km	10~70	14.3~63.0	23.8
H_S , km	10~70	10.1~13.0	10.3
R_{lr}	-1.2~1.2	0.45~1.07	0.87
T , years	300~1400	914~1388	1378
t_{RM} , years	none	153~1181	262
D , km	0~70	4.9~11.3	10.2
t , years	>100	115~638	118
t_{RLC} , years	0~1400	72~1334	None (almost uniform)
d , km	0~10	3.3~7.1	4.6
H_{lr}	-0.85~0.85	0.14~0.68	None

^aThe terms are defined as follows: d , distance south of NATF; H_{lr} , logarithmic thickness ratio of B_N to B_S ; for the definition of other symbols refer to Table 5.

indicates that the northern block (Tarim) is stiffer and thicker compared to the southern block (Qaidam) in order to satisfy the data and reflect the strong asymmetry of strain accumulation. These results are comparable with *Jolivet et al.*'s [2008] from analysis of the same data set using a thin-plate model. They assumed an equal thickness of 11~13 km of the two elastic blocks and found the stiffness ratio of B_N to B_S up to 9. It is, though, widely accepted that the Tarim basin remains relatively undeformed due to the presence of a strong craton during the Cenozoic India-Eurasian collision [*Jolivet et al.*, 2008]. Our result for the stiffness ratio is inclined to the high end of the constraint for the parameter.

[43] An alternative to very high stiffness contrast is to shift the position of the fault from the surface trace of NATF to be closer to the surface trace of SATF. There are some arguments which may support this idea. From geological observations, the SATF might reactivate during the last earthquake with a magnitude of 8 a few hundred years ago [*Mériaux et al.*, 2005]. From seismic tomography, a flower structure might be an expression of the Altyn Tagh fault at shallow depth along some parts of the fault [*Wittlinger et al.*, 1998, 2004]. Therefore, we perform an additional inversion allowing the position of the active fault trace to vary. The result is shown in Table 8. As we would expect, the stiffness ratio of B_N (Tarim) to B_S (Qaidam) decreases. It ranges from 2.8 to 11.7 with a most likely value of 7.4. The shift of fault zone is in a range of 3.3~7.1 km and favors 4.6 km. Thus, we might conclude that the Altyn Tagh fault zone at depth is roughly centered between NATF and SATF. The ranges for other parameters changes accordingly but not dramatically.

[44] The viscosity of the mid-crustal Tibetan channel is not resolvable. However, according to the inversion results for the thickness difference of two elastic layers (Tables 7 and 8), it is likely that there may exist lower crust with low viscosity underneath Qaidam basin because a thinner elastic layer south of ATF (Qaidam basin) is favored.

6. Conclusions

[45] We have developed a new boundary element method for modeling asymmetric interseismic strain accumulation across vertical strike-slip faults due to contrasts in elastic stiffness and thickness across the fault. The method is computationally efficient which allows us to conduct complete inversions for the posterior probability distributions of model parameters. Stiffness and thickness contrasts in elastic plates beside the fault have similar effects on asymmetric strain accumulation. A gentler velocity gradient (lower strain rate) is observed on the side of the stiffer plate or/and thicker plate. However, the role of mantle flow is important. The asymmetry in deformation is strongly enhanced by reducing the shear resistance at the bottom of the elastic plate through relaxing viscous flow. As a consequence, elastic half-space models with bi-material interface may significantly over-predict stiffness contrasts. On the other hand, plate models which neglect coupling at the bottom of the plate [e.g., *Chéry*, 2008] may exaggerate the elastic thickness variations in the crust. Contrasts in elastic thickness produce negligible asymmetry in surface deformation across the fault if the relaxation time of the viscoelastic half-space is long compared to the recurrence time of earthquakes (high viscosity cases in Figure 3). A low-viscosity channel within lower crust

could also significantly contribute to the asymmetry. We found elastic stiffness contrast plays a more important role in the cases with a distinct asymmetric strain pattern than thickness contrast.

[46] The asymmetry across the Renun segment of the Great Sumatra fault requires a stiffness contrast of 2–14, which is lower than the estimate of *Le Pichon et al.* [2005] using an elastic half-space model with bi-material interface. Elastic thickness and stiffness contrast across the Carrizo segment of the San Andreas fault is not resolvable. An elastic stiffness contrast of 3–12 across the Altyn Tagh fault in Tibet is necessary to explain the observed asymmetry. The existence of a low-viscosity lower crust (a channel) in the Tibetan plateau is likely; however, the viscosity of this mid-crustal Tibetan channel is not resolvable.

[47] **Acknowledgments.** This study was supported by Taiwan National Science Council grant NSC100-2116-M-008-002 and U.S. National Science Foundation grant to Indiana University.

References

- Agnew, D. C., and K. E. Sieh (1978), A documentary study of the felt effects of the great California earthquake of 1857, *Bull. Seismol. Soc. Am.*, 68(6), 1717–1729.
- Aldiss, D. T., R. Whandoyo, and A. G. Sjaefudien (1983), Geologic map of the Sidikalang quadrangle, Sumatra, scale 1:250,000, Geol. Res. Div. Cent., Bandung, Indonesia.
- Ampuero, J. P., and Y. Ben-Zion (2008), Cracks, pulses and macroscopic asymmetry of dynamic rupture on a bimaterial interface with velocity-weakening friction, *Geophys. J. Int.*, 173, 674–692, doi:10.1111/j.1365-246X.2008.03736.x.
- Andrews, D. J., and Y. Ben-Zion (1997), Wrinkle-like slip pulse on a fault between different materials, *J. Geophys. Res.*, 102(B1), 553–571, doi:10.1029/96JB02856.
- Bellier, O., and M. Sebrier (1995), Is the slip rate variation on the Great Sumatran fault accommodated by fore-arc stretching?, *Geophys. Res. Lett.*, 22, 1969–1972.
- Ben-Zion, Y., and D. J. Andrews (1998), Properties and implications of dynamic rupture along a material interface, *Bull. Seismol. Soc. Am.*, 88(4), 1085–1094.
- Chéry, J. (2008), Geodetic strain across the San Andreas fault reflects elastic plate thickness variations (rather than fault slip rate), *Earth Planet. Sci. Lett.*, 269, 352–365, doi:10.1016/j.epsl.2008.01.046.
- Crouch, S. L., and A. M. Starfield (1983), *Boundary Element Methods in Solid Mechanics*, Allen and Unwin, Winchester, Mass.
- d'Alessio, M. A., I. A. Johanson, R. Bürgmann, D. A. Schmidt, and M. H. Murray (2005), Slicing up the San Francisco Bay Area: Block kinematics and fault slip rates from GPS-derived surface velocities, *J. Geophys. Res.*, 110, B06403, doi:10.1029/2004JB003496.
- Eissa, E. A., and A. Kazi (1988), Relation between static and dynamic Young's moduli for rocks, *Int. J. Mech. Min. Sci. Geomech. Abstr.*, 25, 479–482, doi:10.1016/0148-9062(88)90987-4.
- Feigl, K. L., et al. (1993), Space geodetic measurement of crustal deformation in central and southern California, 1984–1992, *J. Geophys. Res.*, 98, 21,677–21,712.
- Fialko, Y. (2006), Interseismic strain accumulation and the earthquake potential on the southern San Andreas fault system, *Nature*, 441, 968–971, doi:10.1038/nature04797.
- Field, E. H., et al. (2008), The uniform California earthquake rupture forecast Version 2 (UCERF 2), *U.S. Geol. Surv. Open File Rep.*, 2007-1437, 104 pp.
- Fukuda, J., and K. M. Johnson (2008), A fully Bayesian inversion for spatial distribution of fault slip with objective smoothing, *Bull. Seismol. Soc. Am.*, 98, 1128–1146, doi:10.1785/0120070194.
- Fulton, P., G. Schmalzle, R. Harris, and T. Dixon (2010), Reconciling patterns of interseismic strain accumulation with thermal observations across the Carrizo segment of the San Andreas fault, *Earth Planet. Sci. Lett.*, 300 (3–4), 402–406, doi:10.1016/j.epsl.2010.10.024.
- Ge, S., G. Shen, R. Wei, G. Ding, and Y. Wang (1992), *Active Altun Fault Zone*, 319 pp., State Seismol. Bur. of China, Beijing.
- Genrich, J., Y. Bock, R. McCaffrey, L. Prawirodirdjo, C. Stevens, S. S. O. Puntodewo, C. Subarya, and S. Wdowinski (2000), Distribution of slip at the northern Sumatra fault system, *J. Geophys. Res.*, 105(B12), 28,327–28,341, doi:10.1029/2000JB900158.

- Hearn, E. H., and Y. Fialko (2009), Can compliant fault zones be used to measure absolute stresses in the upper crust?, *J. Geophys. Res.*, *114*, B04403, doi:10.1029/2008JB005901.
- Jackson, D. D., K. Aki, C. A. Cornell, J. H. Dieterich, T. L. Henyey, M. Mahdyar, D. Schwartz, and S. N. Ward (1995), Seismic hazards in southern California—Probable earthquakes, 1994 to 2024, *Bull. Seismol. Soc. Am.*, *85*, 379–439.
- Johanson, I. A., and R. Bürgmann (2005), Creep and quakes on the northern transition zone of the San Andreas fault from GPS and InSAR data, *Geophys. Res. Lett.*, *32*, L14306, doi:10.1029/2005GL023150.
- Johnson, K. M., R. Bürgmann, and J. T. Freymueller (2009), Coupled afterslip and viscoelastic flow following the 2002 Denali Fault, Alaska earthquake, *Geophys. J. Int.*, *176*(3), 670–682, doi:10.1111/j.1365-246X.2008.04029.x.
- Jolivet, R., R. Cattin, N. Chamot-Rooke, C. Lasserre, and G. Peltzer (2008), Thin-plate modeling of interseismic deformation and asymmetry across the Altyn Tagh fault zone, *Geophys. Res. Lett.*, *35*, L02309, doi:10.1029/2007GL031511.
- Lasserre, C., et al. (2007), Interseismic deformation across the Altyn Tagh and Haiyuan faults at the northern edge of the Tibetan plateau, measured by space geodesy, *Geophys. Res. Abstr.*, *9*, 10,102.
- Le Pichon, X., C. Kreemer, and N. Chamot-Rooke (2005), Asymmetry in elastic properties and the evolution of large continental strike-slip faults, *J. Geophys. Res.*, *110*, B03405, doi:10.1029/2004JB003343.
- Lin, G., C. H. Thurber, H. Zhang, E. Hauksson, P. M. Shearer, F. Waldhauser, T. M. Brocher, and J. Hardebeck (2010), A California statewide three-dimensional seismic velocity model from both absolute and differential times, *Bull. Seismol. Soc. Am.*, *100*, 225–240, doi:10.1785/0120090028.
- Lisowski, M., J. C. Savage, and W. H. Prescott (1991), The velocity field along the San Andreas fault in central and southern California, *J. Geophys. Res.*, *96*(B5), 8369–8389, doi:10.1029/91JB00199.
- Liu, J., Y. Klinger, K. Sieh, and C. Rubin (2004), Six similar sequential ruptures of the San Andreas fault, Carrizo Plain, California, *Geology*, *32*, 649–652, doi:10.1130/G20478.1.
- Liu-Zeng, J., Y. Klinger, K. Sieh, C. Rubin, and G. Seitz (2006), Serial ruptures of the San Andreas fault, Carrizo Plain, California, revealed by three-dimensional excavations, *J. Geophys. Res.*, *111*, B02306, doi:10.1029/2004JB003601.
- Lundgren, P., E. A. Hetland, Z. Liu, and E. Fielding (2009), Southern San Andreas-San Jacinto fault system slip rates estimated earthquake cycle models constrained by GPS and Interferometric Synthetic Aperture Radar observations, *J. Geophys. Res.*, *114*, B02403, doi:10.1029/2008JB005996.
- Magistrale, H., S. Day, R. W. Clayton, and R. Graves (2000), The SCEC Southern California reference three-dimensional seismic velocity model Version 2, *Bull. Seismol. Soc. Am.*, *90*(6B), S65–S76, doi:10.1785/0120000510.
- Malservisi, R., K. P. Furlong, and T. H. Dixon (2001), Influence of the earthquake cycle and lithospheric rheology on the dynamics of the eastern California shear zone, *Geophys. Res. Lett.*, *28*(14), 2731–2734, doi:10.1029/2001GL013311.
- McCaffrey, R., P. C. Zwick, Y. Bock, L. Prawirodirdjo, J. F. Genrich, C. W. Stevens, S. S. O. Puntodewo, and C. Subarya (2000), Strain partitioning during oblique plate convergence in northern Sumatra: Geodetic and seismologic constraints and numerical modeling, *J. Geophys. Res.*, *105*(B12), 28,363–28,376, doi:10.1029/1999JB900362.
- McHugh, S., and M. Johnson (1977), Surface shear stress, strain, and shear displacement for screw dislocations in a vertical slab with a shear modulus contrast, *Geophys. J. R. Astron. Soc.*, *49*, 715–722, doi:10.1111/j.1365-246X.1977.tb01314.x.
- Meade, B. J., and B. H. Hager (2005), Block models of crustal motion in southern California constrained by GPS measurements, *J. Geophys. Res.*, *110*, B03403, doi:10.1029/2004JB003209.
- Meade, B. J., B. H. Hager, S. C. McClusky, R. E. Reilinger, S. Ergintav, S. Lenk, A. Barka, and H. Ozener (2002), Estimates of seismic potential in the Marmara Sea region from block models of secular deformation constrained by global positioning system measurements, *Bull. Seismol. Soc. Am.*, *92*(1), 208–215, doi:10.1785/0120000837.
- Mériaux, A.-S., F. J. Ryerson, P. Tapponnier, J. Van der Woerd, R. C. Finkel, X. Xu, Z. Xu, and M. W. Caffee (2004), Rapid slip along the central Altyn Tagh Fault: Morphochronologic evidence from Cherchen He and Sulamu Tagh, *J. Geophys. Res.*, *109*, B06401, doi:10.1029/2003JB002558.
- Mériaux, A.-S., et al. (2005), The Aksay segment of the northern Altyn Tagh fault: Tectonic geomorphology, landscape evolution, and Holocene slip rate, *J. Geophys. Res.*, *110*, B04404, doi:10.1029/2004JB003210.
- Meyer, B., P. Tapponnier, Y. Gaudemer, G. Peltzer, S. M. Guo, and Z. T. Chen (1996), Rate of left-lateral movement along the easternmost segment of the Altyn Tagh fault, east of 96E (China), *Geophys. J. Int.*, *124*(1), 29–44, doi:10.1111/j.1365-246X.1996.tb06350.x.
- Mitchell, T. M., Y. Ben-Zion, and T. Shimamoto (2011), Pulverized fault rocks and damage asymmetry along the Arima-Takatsuki Tectonic Line, Japan, *Earth Planet. Sci. Lett.*, *308*, 284–297, doi:10.1016/j.epsl.2011.04.023.
- Mosegaard, K., and A. Tarantola (2002), Probabilistic approach to inverse problems, in *International Handbook of Earthquake and Engineering Seismology, Part A*, edited by W. H. K. Lee et al., pp. 237–265, Academic, San Diego, Calif., doi:10.1016/S0074-6142(02)80219-4.
- Page, B. M. (1981), *The Southern Coast Ranges*, Prentice Hall, Upper Saddle River, N. J.
- Peltzer, G., P. Tapponnier, and R. Armijo (1989), Magnitude of late Quaternary left-lateral displacements along the north edge of Tibet, *Science*, *246*, 1285–1289, doi:10.1126/science.246.4935.1285.
- Pollitz, F. F., P. Banerjee, and R. Bürgmann (2006), Postseismic relaxation following the great 2004 Sumatra-Andaman earthquake on a compressible self-gravitating earth, *Geophys. J. Int.*, *167*, 397–420, doi:10.1111/j.1365-246X.2006.03018.x.
- Pollitz, F. F., P. McCrory, J. Svarc, and J. Murray (2008), Dislocation models of interseismic deformation in the western United States, *J. Geophys. Res.*, *113*, B04413, doi:10.1029/2007JB005174.
- Pollitz, F. F., P. McCrory, D. Wilson, J. Svarc, C. Puskas, and R. B. Smith (2010), Viscoelastic-cycle model of interseismic deformation in the northwestern United States, *Geophys. J. Int.*, *181*, 665–696, doi:10.1111/j.1365-246X.2010.04546.x.
- Rybicki, K., and K. Kasahara (1977), A strike-slip in a laterally in homogeneous medium, *Tectonophysics*, *42*, 127–138, doi:10.1016/0040-1951(77)90164-0.
- Schmalzle, G., T. Dixon, R. Malservisi, and R. Govers (2006), Strain accumulation across the Carrizo segment of the San Andreas Fault, California: Impact of laterally varying crustal properties, *J. Geophys. Res.*, *111*, B05403, doi:10.1029/2005JB003843.
- Segall, P. (2010), *Earthquake and Volcano Deformation*, Princeton Univ. Press, New Jersey.
- Sieh, K. E., and R. H. Jahns (1984), Holocene activity of the San Andreas Fault at Wallace Creek, California, *Geol. Soc. Am. Bull.*, *95*, 883–896, doi:10.1130/0016-7606(1984)95<883:HAOTSA>2.0.CO;2.
- Sieh, K., and D. Natawidjaja (2000), Neotectonics of the Sumatran fault Indonesia, *J. Geophys. Res.*, *105*(B12), 28,295–28,326, doi:10.1029/2000JB900120.
- Sieh, K., J. Rais, and Y. Bock (1991), Neotectonic and paleoseismic studies in west and north Sumatra, *Eos Trans. AGU.*, *72*(44), 460.
- Tapponnier, P., and P. Molnar (1977), Active faulting and tectonics in China, *J. Geophys. Res.*, *82*(20), 2905–2930, doi:10.1029/JB082i020p02905.
- Vaghri, A., and E. H. Hearn (2012), Can lateral viscosity contrasts explain asymmetric interseismic deformation around strike-slip faults?, *Bull. Seismol. Soc. Am.*, *102*(2), 490–503, doi:10.1785/0120100347.
- Van der Woerd, J., X. Xu, H. B. Li, P. Tapponnier, B. Meyer, F. J. Ryerson, A. S. Meriaux, and Z. Q. Xu (2001), Rapid active thrusting along the northwestern range front of the Tanghe Nan Shan (western Gansu, China), *J. Geophys. Res.*, *106*(B12), 30,475–30,504, doi:10.1029/2001JB000583.
- Washburn, Z., J. R. Arrowsmith, S. L. Forman, E. Cowgill, X. F. Wang, Y. Zhang, and Z. G. Chen (2001), Late Holocene earthquake history of the central Altyn Tagh fault, China, *Geology*, *29*(11), 1051–1054, doi:10.1130/0091-7613(2001)029<1051:LHEHOT>2.0.CO;2.
- Wittlinger, G., P. Tapponnier, G. Poupinot, J. Mei, S. Danian, G. Herquel, and F. Masson (1998), Tomographic evidence for localized lithospheric shear along the Altyn Tagh Fault, *Science*, *282*, 74–76, doi:10.1126/science.282.5386.74.
- Wittlinger, G., J. Vergne, P. Tapponnier, V. Farra, G. Poupinot, M. Jiang, H. Su, G. Herquel, and A. Paul (2004), Teleseismic imaging of subducting lithosphere and Moho offsets beneath western Tibet, *Earth Planet. Sci. Lett.*, *221*, 117–130, doi:10.1016/S0012-821X(03)00723-4.
- Yeats, R., K. Sieh, and C. Allen (1997), *The Geology of Earthquakes*, 568 pp., Oxford Univ. Press, New York.
- Zaliapin, I., and Y. Ben-Zion (2011), Asymmetric distribution of aftershocks on large faults in California, *Geophys. J. Int.*, *185*, 1288–1304, doi:10.1111/j.1365-246X.2011.04995.x.
- Zhang, P.-Z., P. Molnar, and X. Xu (2007), Late Quaternary and present-day of slip along the Altyn Tagh Fault, northern margin of the Tibetan Plateau, *Tectonics*, *26*, TC5010, doi:10.1029/2006TC002014.
- Zhu, L., and H. Kanamori (2000), Moho depth variation in southern California from teleseismic receiver functions, *J. Geophys. Res.*, *105*(B2), 2969–2980, doi:10.1029/1999JB900322.